CHAPTER 5

DESIGN AND SIMULATION INVESTIGATION OF PERIODIC DIELECTRIC LOADED SECOND HARMONIC GYRO-TWT

5.1. Introduction

Gyro-TWT amplifier exploits the convective instability of the relativistic CRM mechanism that leads to the amplification of RF wave for a wider range of frequency. At low cyclotron harmonic operation, the high power-handling capability of the device is offset by the requirement of high magnetic (B) field. On the other hand, the lower order mode of operation at higher frequencies reduces the physical dimension of the RF interaction circuit hence limiting its power handling capability. The operation of gyro-TWT at harmonics with higher order mode is one of the effective methods to overcome these obstacles and get high output power at higher frequencies. The beam synchronism (5.1) states that as the cyclotron resonance frequency (Ω_c) increases, so does the requirement of magnetic field (B).

$$\omega \approx k_z v_z + s\Omega_c \tag{5.1}$$

where, ω is operating frequency, 's' is the harmonic order. The requirement of magnetic field $B\,(T) \cong f\,(GHz)/(28 \times s)$ is reduced to 1/s times by operating the device at s^{th} harmonic. Also, the waveguide radius (r_w) is directly proportional to the eigenvalue (χ_{mn}) of the operating mode, which is given as,

$$r_w\,(\text{mm}) = \frac{300 \times \chi_{mn}}{2\pi\,f\,(GHz)} \tag{5.2}$$

The higher order mode operation can increase the transverse dimension of the circuit; hence high-power handling capability of the device is achieved. The beam wave interaction weakens rapidly as the harmonic order increases therefore, harmonic operation yields higher stability and high oscillation threshold current than the fundamental harmonic operation. However, the mode competition problem is more severe than the fundamental harmonic operation.

In the present chapter, a periodic dielectric disc loaded RF interaction structure along with an RF input/output system are employed to study the second harmonic higher order TE$_{02}$ mode of operation of gyro-TWT. The rest of the chapter is organized as follows: Section 5.2 discusses the design of triode electron gun and its sensitivity analysis and the design of a novel gradually tapered TE_{02} mode convertor is discussed. In section 5.3, the detailed analysis and design of periodic dielectric loaded waveguide for harmonic gyro-TWT, stability against BWOs, and beam-wave interaction are discussed. Section 5.4 discusses the PIC simulation results and parametric study of beam wave interaction structure for second harmonic W-band gyro-TWT. Section 5.5 deals with the design and simulation study of undepressed conventional and curved collectors and double disk microwave output window and finally the conclusion is drawn in section 5.6.

5.2. Input System of Second Harmonic Gyro-TWT

A double anode or triode magnetron injection gun (MIG) to produce a gyrating electron beam of 100 kV and 25A is designed and simulated using electron optics, *i.e.* EGUN. To drive the operating TE$_{02}$ mode at the input of RF interaction circuit a $TE_{10}^{\square} - TE_{01}^{\circ} - TE_{02}^{\circ}$ mode convertor is designed and cold simulated using 'CST Transient Solver'.

5.2.1. Double Anode Magnetron Injection Gun

A double anode (triode type) magnetron injection gun (MIG) is chosen for the present second harmonic gyro-TWT because it allows more parameter space to adjust the electron momentum due to an additional control voltage. The desired electron beam parameters such as beam voltage and beam current are calculated based on the required output power and efficiency. The initial MIG design parameters including emitter radius

100

Table 5.1: Optimzed Design and Simulated Parameters of Triode MIG.

Design parameters	Value
Main anode voltage, V_0	100 kV
Beam Current, I_0	25 A
Modulating anode voltage, V_a	59 kV
Emitter radius, r_c	8.0 mm
Slant length, l_s	5.4 mm
Slant angle, φ_c	50^0
Cathode Magnetic field, B_c	610 Gauss
Compression ratio, F_m	30
SIMULATED RESULTS OF TRIODE MIG	
Velocity ratio, α	1.22
Axial velocity spread, $\delta\beta_z$	4.0 %
Average beam radius, r_g	1.55 mm
Current density, J_c	6.8 A /cm^2

anode cathode gap, slant angle, slant length, and cathode magnetic field are calculated by using the analytical trade-off equations [Baird *et al*. (1986)]. Figure 5.1(a) shows the variation of compression ratio (F_m) and magnetic field (B_c) at the cathode with respect to the emitter radius (r_c). As r_c increases, F_m is increased but B_c is decreased. The slant length (l_s) is also decreased nonlinearly with respect to r_c [Figure 5.1(b)]. After getting the set of initial MIG parameters, it is modeled and simulated using a commercially available E-GUN code [Herrmannsfeldt (1988)], to get the final optimized MIG geometry and the desired beam parameters. The initial design parameters and simulated results are shown in Table 5.1. Figure 5.2 shows the 2D geometry of the present MIG, magnetic field profile and the simulated electron beam trajectory. The annular electron beam is getting compressed along the axial length by adiabatically increasing the B-field. The ratio of the magnetic field at the interaction circuit and at the cathode is calculated as 30. The post-processing program 'PPGYRO' is used to calculate the
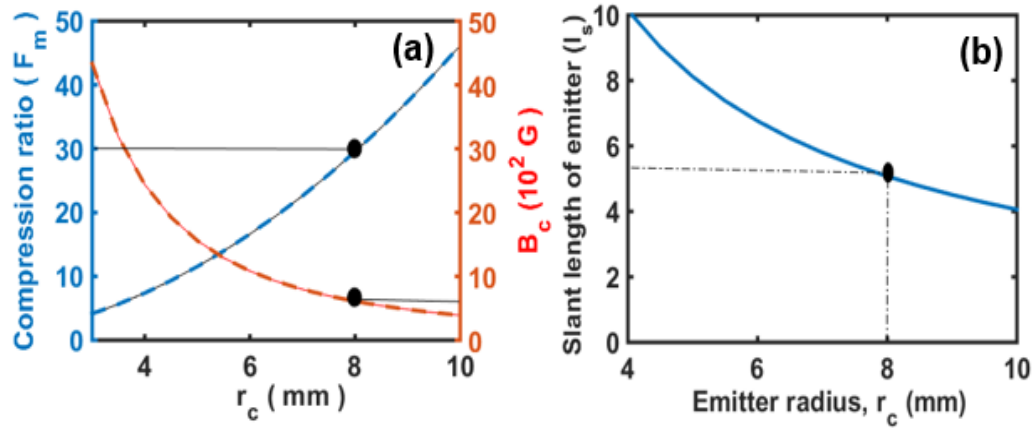
Figure 5.1 (a) Magnetic compression ratio and magnetic field at the cathode as a function of cathode radius r_c (b) slant length of the emitter strip as a function of emitter radius r_c.
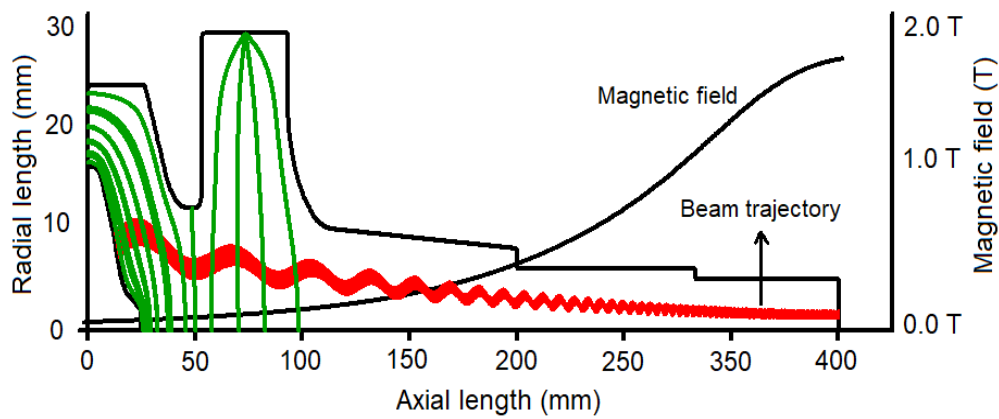

Figure 5.2 The triode MIG geometry, beam trajectory and magnetic field profile along the axial length using EGUN code.
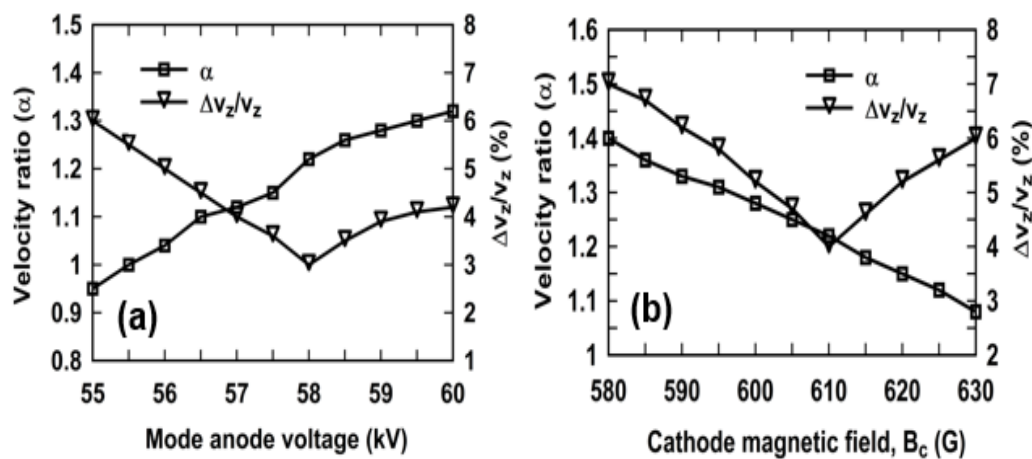

Figure 5.3 Axial velocity spread and velocity ratio as a function of (a) mod-anode voltage, V_a (kV) and (b) cathode magnetic field B_c (Gauss).

102

desired beam quality with velocity ratio of ~1.22 and minimum axial velocity spread (AVS) ~ 4 %. Since, the electronic efficiency of gyro-TWT is very sensitive to the quality of electron beam, even a small change in MIG parameters can lead to the undesired result. Therefore, sensitivity analysis of MIG parameters including modulating anode voltage (V_a) and cathode magnetic field (B_c) is carried out. Figure. 5.3(a) shows that α increases lineally, as V_a is varied from 55 kV to 60 kV. The AVS decreases linearly from 6 % to 3.8 %, as V_a is varied from 55 kV and beyond 58 kV the AVS grows slightly. The AVS and α are observed highly sensitive to cathode magnetic field (B_c). As B_c is varied from 580 G to 630 G, α is varied inversely from 1.4 to 1.1. The AVS is decreased from 7.5% to 3.9%, as B_c changes from 580 G to 610 G, and then increased up to 5.5%, as B_c varies from 610 G to 630G [Figure 5.3(b)].

5.2.2. Design of TE_{02} Mode Input Coupler

An RF input coupler is designed and simulated to launch the desired higher order TE_{02} operating mode into the interaction region. The present rectangular TE_{10} mode to circular TE_{02} mode input coupler consists of three sections: (i) a cascaded Y-shaped power divider TE_{10} to TE_{01} mode convertor, (ii) a gradually tapered slotted waveguide section, and (iii) a TE_{02} mode output waveguide [Figure. 5.4(a)]. In section-I, the rectangular TE_{10} mode is divided into four signals with equal amplitude and 90^0 phase difference through a cascaded Y-shaped power divider. These four signals are fed to the circular waveguide through side-wall coupling method to form the circular TE_{01} waveguide mode [Yu *et al.* (2005), Akash *et al.* (2019)]. Section-II is gradually tapered slotted waveguide section, which is basically converts the lower order azimuthal symmetric mode into the next higher order azimuthal symmetric mode. It consists of a circular waveguide of radius r_1 and N number of slotted waveguides. At a fixed axial
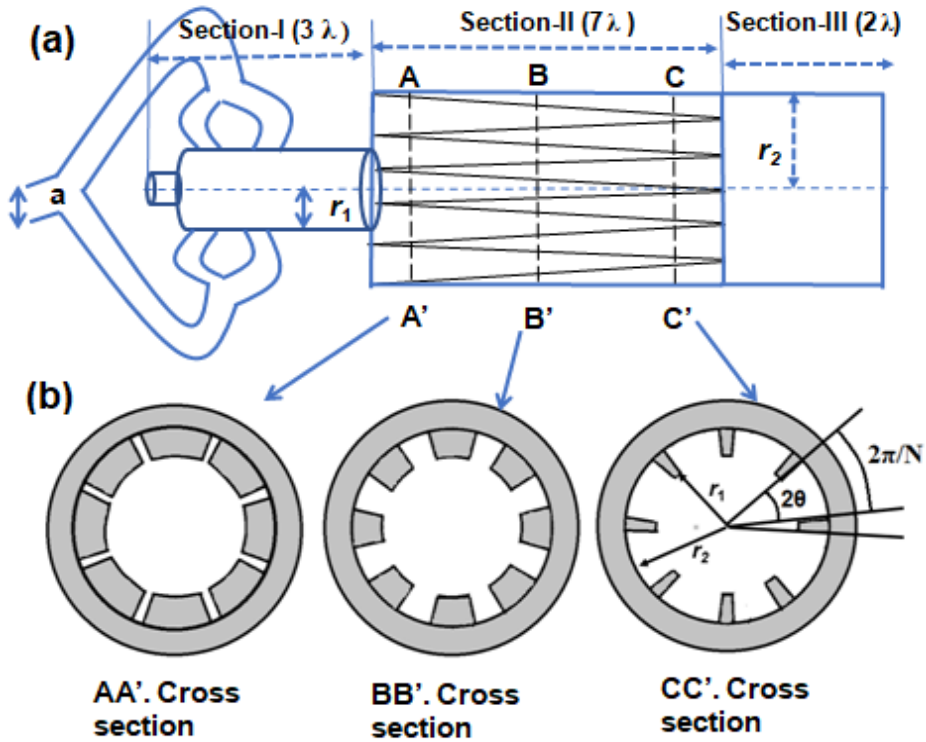
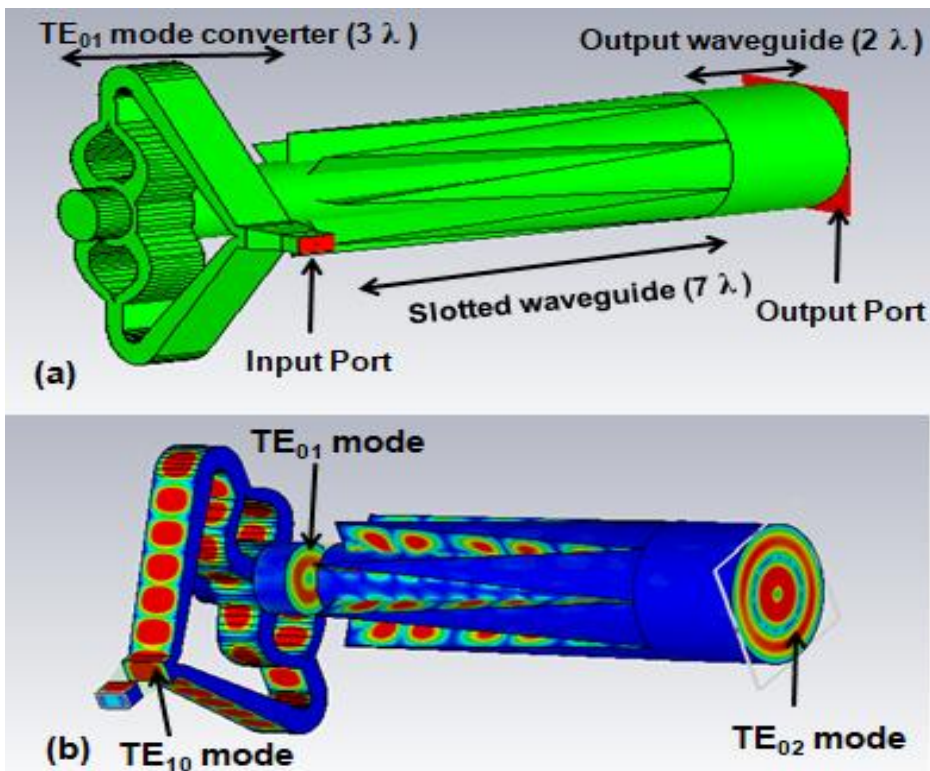**Figure 5.4** (a) Schematic of TE_{02} mode input coupler and (b) cross-sectional view at different axial positions.

Figureure 5.5 (a) CST model of the TE_{02} mode convertor modeled as vacuum, (b) axial view of electric field distribution inside mode convertor.
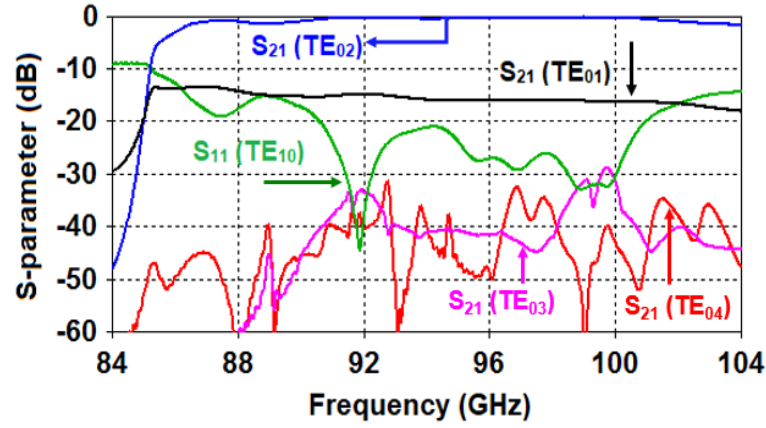
Figure 5.6 The S-parameter results of TE_{02} mode input coupler.

position, the angle of separation between each slot is 2θ, which varies from 0 to $2\pi/N$ with the variation in axial length from L_1 to L_2 [Figure. 5.4(a)]. The depth $(r_2 - r_1)$ of each slotted waveguide is kept constant and chosen in such a way that to satisfy the following condition [Guo *et al*. (1990)],

$$\chi_{0n}/r_1 = \chi_{0,n+1}/r_2 = k_{c0}, \quad J_0'(\chi_{0n}) = J_0'(\chi_{0n+1}) = 0 \tag{5.3}$$

where, n is an integer value and represent the azimuthal wavenumber of the azimuthally symmetric mode, r_1 and r_2 are the radii of the uniform waveguides, χ_{0n} and χ_{0n+1} are n^{th} and $(n+1)^{th}$ root of $J_0'(\chi) = 0$, respectively, and $J_0'(\chi)$ is the derivative of first kind, zeroth order Bessel function. The lengths of all three sections are 3λ, 7λ, 2λ, respectively (where, λ is the operating wavelength). According to equation (5.3), the TE_{02} mode converting section can be approximated to a section of uniform waveguide having a characteristic wave number, k_{c0}. There must be minimum reflection of wave due to the continuous k_{c0} throughout the mode converting section. The modes that having radial component of electric field will not be excited due to very thin radial sheet of metal at one end. Hence, the mode convertor can also act as a mode filter. On the other hand, due to the relation in equation (5.3), there will not be any conversion of modes except for TE_{0n} and $TE_{0, n+1}$, *i.e.*, the propagation of non-azimuthal symmetric modes is restricted. The present TE_{10}—TE_{01}—TE_{02} mode convertor [Figure. 5.5(a)] is modeled in

105

a commercially available electromagnetic code "CST Microwave Studio". Figure. 5.5(b) depicts the electric field distribution of TE_{10}, TE_{01} and TE_{02} mode at the input port, at the end of section I, and at the output port, respectively. Figure 5.6 shows the cold simulation results of the present input coupler, which includes the reflection (S_{11}) at the input port, transmission (S_{21}) of the desired TE_{02} and competing modes. The reflection is less than -20 dB over the frequency band of interest and the TE_{01} mode is found to be most competing mode and the conversion of input power into TE_{01} mode is well below -16 dB throughout the operating frequency band. The conversion into other competing modes is well below -30dB. The transmission of the operating TE_{02} mode is better than -0.2 dB over the frequency band of 90-100 GHz.

5.3. Design of Beam Wave Interaction Structure

The periodic dielectric loaded interaction waveguide is employed for the second harmonic W-band gyro-TWT operation. A weak electric and high thermal conductive lossy dielectric material 'BeO-TiO2-W' is used to heavily attenuate the oscillating and competing modes. The weight percentage of beryllium oxide (BeO), titanium dioxide (TiO2) and tungsten are 75%-20%-5%. The analytical modeling of the interaction structure, beam wave coupling strength analysis for second harmonic operation and stability analysis of second harmonic gyro-TWT are discussed in this section.
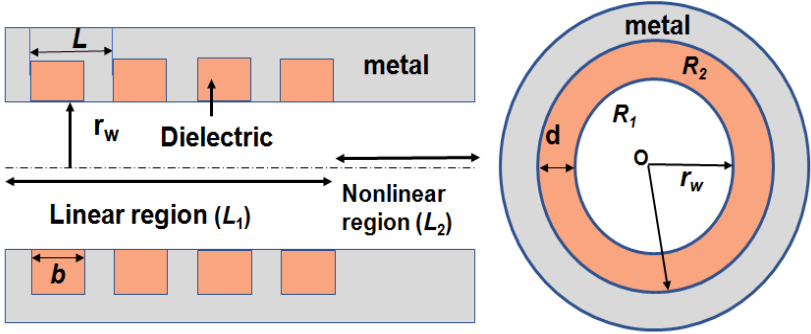

Figure 5.7 The Axial and transverse schematic view of periodic dielectric loaded waveguide.

106

5.3.1. Analytical Model of Interaction Waveguide

The present periodic dielectric loaded (PDL) RF interaction waveguide (Figure 5.7) for second harmonic gyro-TWT consists of two regions. The inner waveguide region R_1 ($0 \leq r < r_w$ and $0 \leq z < \infty$) is the inner vacuum region, and region R_2 ($r_w \leq r < r_D$ and $0 \leq z < b$) is the lossy dielectric region. The boundary conditions for the PDL waveguide structure is discussed in previous chapter.

5.3.2. Dispersion and Beam-Wave Coupling Analysis

The beam-wave interaction impedance is used to describe the coupling strength of electron beam with the waveguide modes. The coupling impedance in a gyro-TWT can be defined as [Du *et al*. (2014)],

$$K = \frac{|\mathrm{U}|^2}{2P} = \mu_1 \frac{H_{sm}}{G_V + G_D} \frac{r_L^2}{s^2} \upsilon_p \tag{5.8}$$

where, P is the power flow in the circuit and K is the impedance at any point in the circuit, U is the RF equivalent voltage, $H_{sm} = |J'_m(k_{t1}r_L)J_{m-s}(k_{t1}r_g)|^2$ is the coupling factor, 's' is the harmonic order, v_p is the phase velocity of the wave, which depends on the axial wave number as $v_p = \omega / k_z$, G_V and G_D are the geometry factors in vacuum and dielectric regions, respectively. Figure 5.8(a) and 5.8(b) show the mesh plot of H_{sm} as a function of the normalized guiding center and Larmor radii for the fundamental and second harmonic TE$_{02}$ mode. It is observed that the H_{sm} for the second harmonic is weaker than the fundamental harmonic operation. It shows that as the harmonic order increases the coupling strength decreases. Also, H_{sm} is a decreasing function of the normalized Larmor radius, for $s = 1$ and increasing function of the normalized Larmor radius, for $s = 2$. For the maximum beam-wave coupling, the beam position should be at the maximum of electric field component of the operating waveguide mode. Figure 5.9
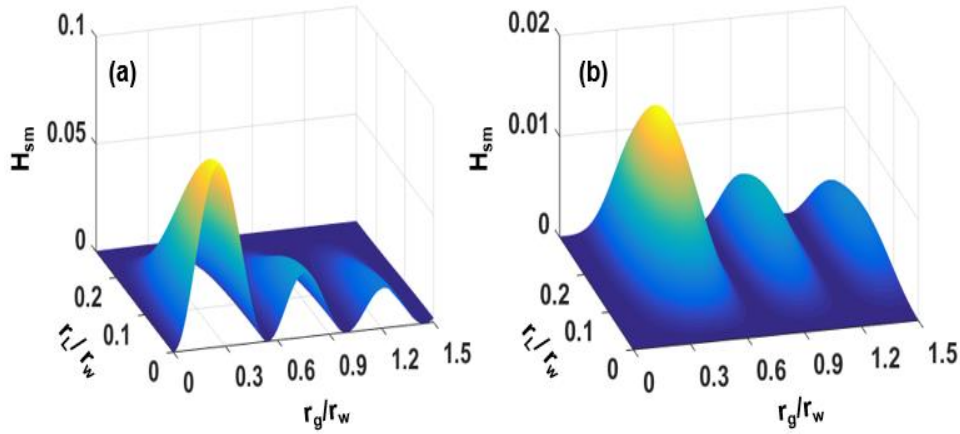
Figure 5.8 Coupling coefficient, H_{sm} of the TE_{02} mode at (a) fundamental and (b) second Harmonic operation.
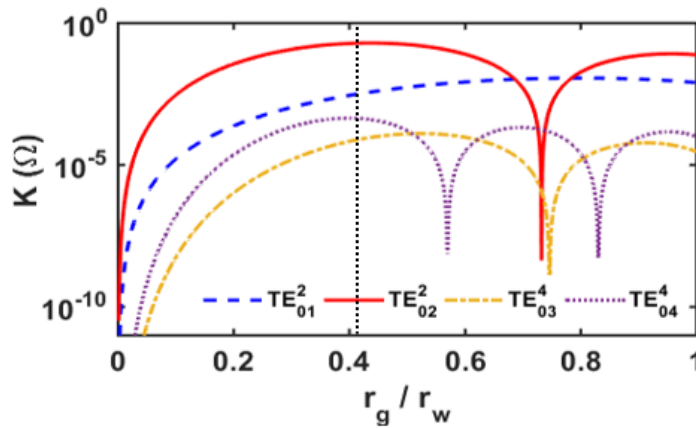

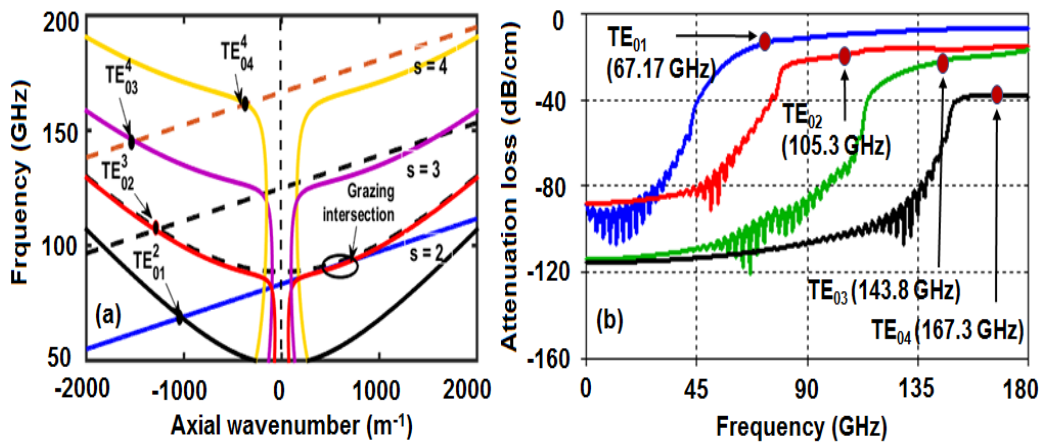**Figure 5.9** Coupling impedance Vs normalized guiding center radius.

Figure 5.10 (a) Dispersion diagram of operating and competing modes for W-band gyro-TWT. (b) Attenuation loss to the operation TE_{02} mode and potential BWOs in the dielectric waveguide.
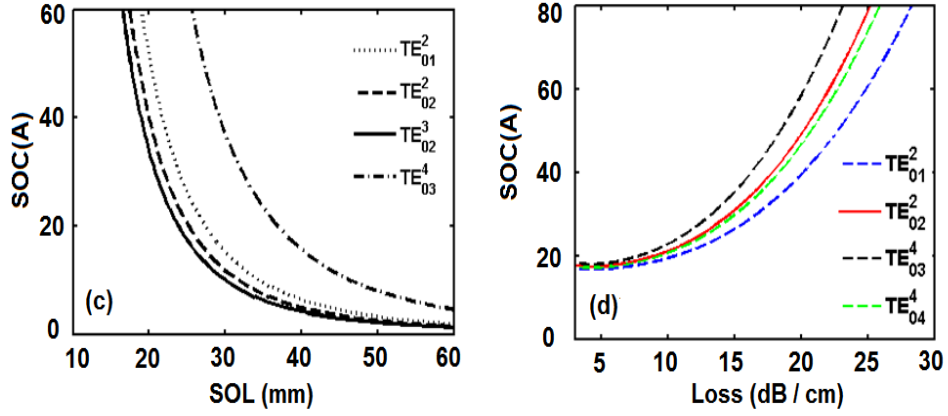
108

Figure 5.11 (a) SOC Vs SOL of operating mode and potential BWO modes in unloaded section (b) SOC of operating and BWO modes as a function of loss in dB /cm.

shows the coupling impedance (K) for the operating and possible competing modes as a function of the normalized beam guiding center radius. The maximum coupling impedance is obtained at $0.44*r_w$. To avoid the mode competition by weakening the coupling impedance of competing TE_{01}^2, TE_{02}^3, TE_{03}^4 and TE_{04}^4 modes, the value of coupling impedance $0.41*r_w$ has been chosen for the present design [Wang *et al.* (2000)]. However, the coupling impedance of the operating TE_{02} mode is still maximum.

5.3.3. Study of BWOs and Stability Analysis

The dispersion diagram [Figure 5.10(a)] of the second harmonic TE_{02} mode gyro-TWT interaction for the beam parameter of 100 kV, 25 A and velocity ratio of 1.22 has been plotted. It is well understood that intersection point of the lossy waveguide modes with the fundamental or harmonic beam mode lines in the backward wave region (negative k_z) are the potential threat of absolute instability. The dispersion diagram shows that TE_{01}^2, TE_{02}^3, TE_{03}^4 and TE_{04}^4 modes, are the possible spurious oscillating modes (superscript denotes the harmonic number). To suppress these modes effectively a PDL interaction circuit is chosen. The lossy ceramic BeO-TiO2-W (75% - 20% - 5%) with high thermal conductivity and low electrical conductivity is used. The

109

low electrical conductivity of the material is chosen to reduce the problem of dielectric charging [21]. The attenuation characteristics of the operating and other oscillating modes in the PDL interaction circuit are calculated. It is observed from Figure 5.10(b) that a loss of ~15.7dB /cm to the second harmonic (s = 2) TE_{01} mode at ~67.17GHz, ~19.3dB /cm to the third harmonic (s = 3) TE_{02} mode at ~105.3GHz, ~22.6dB /cm to the fourth harmonic (s = 4) TE_{03} at ~143.8GHz, and ~37.7dB /cm to the fourth harmonic (s = 4) TE_{04} at ~167.3GHz is introduced by the chosen lossy dielectric material. To improve the stability of gyro-TWT, the length of the unloaded section of RF interaction waveguide is kept smaller than the start oscillation length (SOL) of spurious modes. The linear theory [Kou *et al.* (1992)] is used evaluate the SOL [Figure 5.11(a)] of spurious modes. It is observed that at a beam current of 25A, SOL of the operating TE_{02} mode is 2.45cm, while TE_{02} mode at $s = 3$ has SOL of 2.2 cm that is least among all other spurious modes. For the stable operation, the length of the unloaded section must be less than 2.2cm. In the present design, an unloaded section with an optimized length of 1.95 cm is chosen. The start oscillation current (SOC) of the operating mode at this length is ~40A well above the operating current. To achieve the desired amplification and gain, the length of RF circuit is increased by adding a lossy linear section. The lossy section has reduced the strength of spurious modes by introducing sufficient attenuation, hence their SOC is increased. Figure 5.11(b) shows that SOC of both the operating and competing modes increases exponentially with respect the loss in dB /cm. At their respective attenuation loss, SOC of the operating as well as spurious modes is well above the operating current, for example at 19.3dB /cm of loss, SOC of the TE_{02} mode is increased to ~45A.

5.4. PIC Simulation and Validation

The proposed PDL RF interaction circuit is modeled using Finite Integration Technique (FIT) based 3D electromagnetic code "CST Particle Studio" to study the beam wave interaction behavior of the present W-band second harmonic gyro-TWT [Figure 5.12]. Both structural and electrical parameters of the present gyro-TWT are listed in Table 5.2. The gyrating electron beam of 100kV, 25A with the velocity ratio of ~1.22 and ~4% axial velocity spread is emitted from the cylindrical cathode. The amplified E-field and corresponding output power in the operating TE_{02} mode is shown in Figures 5.13(a) and 5.13(b), respectively. The PIC simulation predicted a saturated RF output power of ~490kW at 91.4GHz. The Fourier Transform (inset) of the amplified signal confirms the frequency of the developed operational TE_{02} mode of the present gyro-TWT as ~92GHz. The signal developed in competing modes are also observed *i.e.*, TE_{01} mode at ~67GHz, TE_{03} mode at ~144GHz and TE_{04} mode at ~173GHz. However, their relative field strength is lower than the field strength of operating TE_{02} mode by ~60dB, ~70dB and ~68dB, respectively. This shows that the competing modes are effectively suppressed by the lossy dielectrics loaded in the waveguide. The PIC simulation results are compared with the existing nonlinear theory [Du *et al.* (2014)] of gyro-TWT for different frequencies ranging from 90GHz to 98GHz [Figure 5.14(a)]. Both of the results are agreed well within ~4%. The transfer characteristics [Figure 14(b)] of the device for 0% and 4% axial beam velocity spread shows that as the input power is varied from 300W to 700W with a step size of 50W, the output power is increased almost linearly and maximum output power is achieved at 600 W of input power. The RF output and efficiency of the present second harmonic gyro-TWT are observed with respect to the operating frequency for various axial velocity spread. The simulation predicted a 3-dB bandwidth and maximum efficiency of

111

4.8GHz and 24%, respectively, for 0% axial velocity spread, and 3.6GHz and ~20%, respectively for 4% axial velocity spread. The performance of the second harmonic gyro-TWT is also observed with respect to the operating frequency for various axial velocity spread. The simulation predicted a 3-dB bandwidth of 4.2GHz and 3.3GHz for an axial velocity spread of 0 % and 4%, respectively.
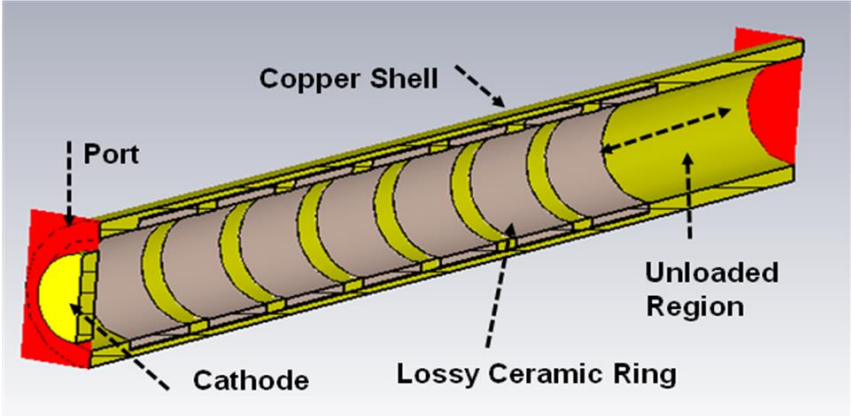

Figure 5.12 CST model of periodically dielectric loaded waveguide for second harmonic TE_{02} mode W-band gyro-TWT.
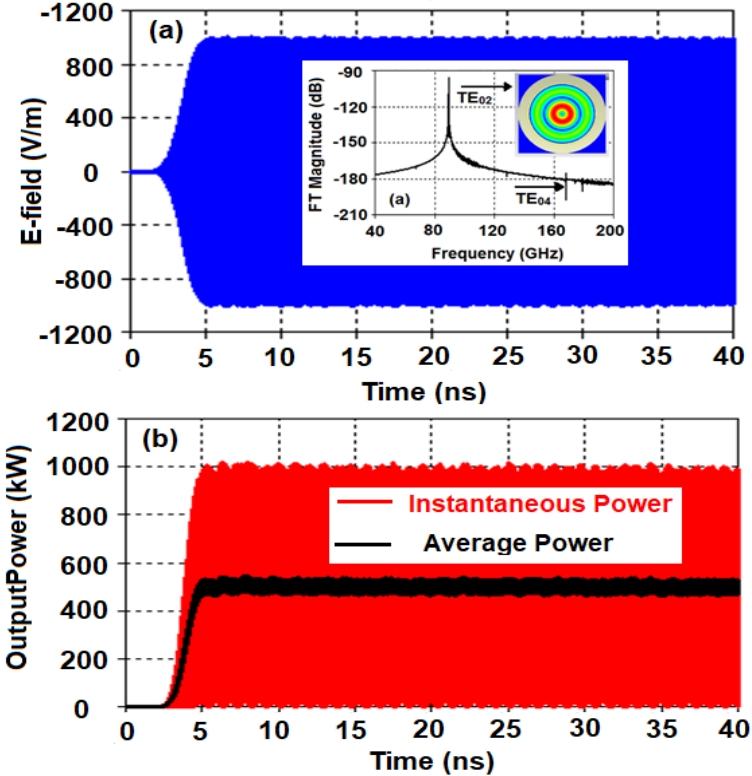

Figure 5.13 (a) Amplified electric field and (b) output power of TE_{02} mode at the output port.
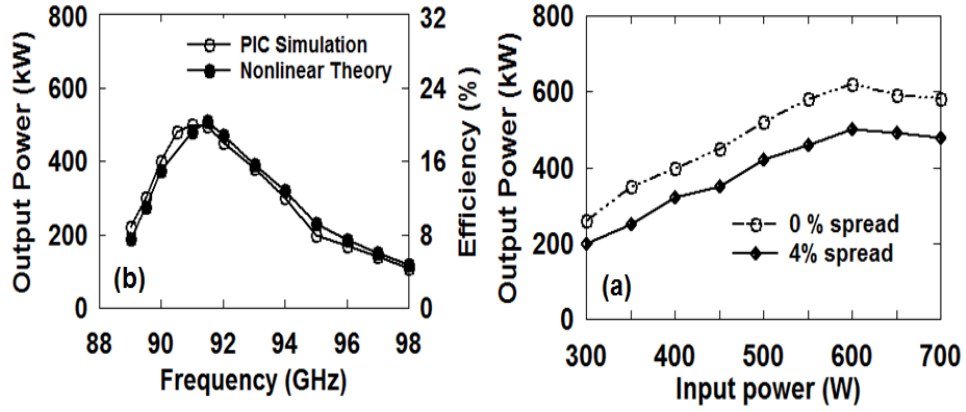
Figureure 5.14 (a) Comparison of PIC simulation results with nonlinear theory. (a) Transfer characteristic of present gyro-TWT for 0% and 4% axial velocity spread.

Table 5.2: Design Parameters of W-band 2nd Harmonic gyro-TWT

Parameters	Values
Beam Voltage (V)	100 kV
Beam Current (I)	25 A
Velocity Pitch Factor (α)	1.22
Operating Mode	TE_{02}
Harmonic Number	Second
Cut-off Frequency	88.6 GHz
Lossy dielectric	BeO-TiO2-W
DC Magnetic Field, B_0	1.785T
Total Lossy section length (L_1)	8.0cm
Copper circuit length (L_2)	1.5 cm
Total circuit length	9.5 cm

5.5.   Output System of Second Harmonic gyro-TWT

A curved collector is designed and simulated using electron optics (EGUN). The curve geometry of the collector is chosen to reduce the heat wall loading at the collector wall due to the dumping of spent electron beam with high energy. A double disk window for the extraction of the amplified TE$_{02}$ mode RF power is also designed and studied using both analytical and simulation methods.

5.5.1. Design of Curved Collector

The normal beam collector has limited power dissipation capability as the electron beam distributed over a focused area and its simple cylindrical waveguide

geometry of constant radius [Akash *et al.* (2019)]. Therefore, a curved collector is designed for the present gyro-TWT to collect the spent electron beam with low heat wall loading. The curved geometry will allow the beam to spread over the large area and hence increases the power handling capability of the collector [Jiang *et al.* (2014)]. In the undepressed collector, the kinetic energy of the spent electrons is totally converted into thermal energy and therefore collector must dissipate it as heat effectively. The performance of the collector is evaluated by the heat dissipating capability of the collector surface. For the copper material, the heat wall loading in the collector region should be less than 2.0kW /cm^2. For the DC beam power of 2.5MW and maximum efficiency of 24%, the present collector must handle kinetic beam power of ~190kW (considering 10 % duty cycle). The beam radius in the collector region of gyro-TWT can be expressed as [Jiang *et al.* (2014)],

$$r = r_{gc} + r_L \cos\theta = \sqrt{\frac{B_0}{B(z)}}\, r_{g0} + \frac{\gamma m \upsilon_t}{e}\sqrt{B(z)B_0}\,\cos\theta_0 \qquad (5.9)$$

where, r_{g0}, υ_t, θ_0, and B_0 are the guiding center radius, transverse velocity, phase of electron, and magnetic field at the end of RF circuit, respectively, r_{gc}, r_L, and $B(z)$ are the guiding center radius, Larmor radius, and magnetic field at a specific position in the collector region. The phase of electron (θ_0) is an important factor in equation (5.9). This implies that with the same guiding center and Larmor radii but at different phases in the gyro-orbit, electrons will not be intercepted by the collector at the same axial position. The magnetic field strength in the beam dump region of collector is decreased from 160 Gauss to 100 Gauss and the average beam radius of ~22mm is chosen. 2D geometry, magnetic field strength, and trajectory of the electron beam of both conventional and curved collectors are shown in Figures 5.15(a) and 5.15(b), respectively. The radii of the collector (r_1) and output window (r_2) are calculated as 22.0mm and 9.0mm,

respectively. The spent electron beam is distributed over ~230mm and ~370mm length in conventional [Figure 15(a)] and curved [Figure 5.15(b)] collectors, respectively. Therefore, the heat dissipating area of the curved collector is larger than conventional collector, hence higher the heat dissipation capability. The maximum heat wall loading of the normal and curved collectors is calculated as ~0.597kW/ cm^2 and ~0.39kW /cm^2, respectively.

The variation in radius of the collector region may affect the wave propagation, which may be reflecting partially into the RF interaction region and causes the oscillations in the device. Therefore, the collector region must have high transmission and low reflection characteristics. To analyze the transmission and reflection performance of the conventional and curved collectors, both are cold simulated using 'CST Microwave Studio'. Figure 5.16(a) shows the electric field distribution for the TE$_{02}$ mode in the conventional collector region. The mode pattern is quite acceptable over the entire length of the collector. As shown in Figure 5.16(b), the reflection coefficient (S_{11}) of TE$_{02}$ mode is less than −20.7dB, and S_{21} is better than −0.1dB over the frequency band of 90 to 98GHz. Similarly, the electric field distribution for the TE$_{02}$ mode in the curved collector region is shown in Figure 5.16(c). The mode pattern seems to be more pure than conventional one over the entire length of the collector. In the curved collector, the reflection coefficient (S_{11}) of TE$_{02}$ mode is less than −32.6dB, and S_{21} is better than −0.04dB over the frequency band of 90 to 98GHz [Figure 5.16(d)].
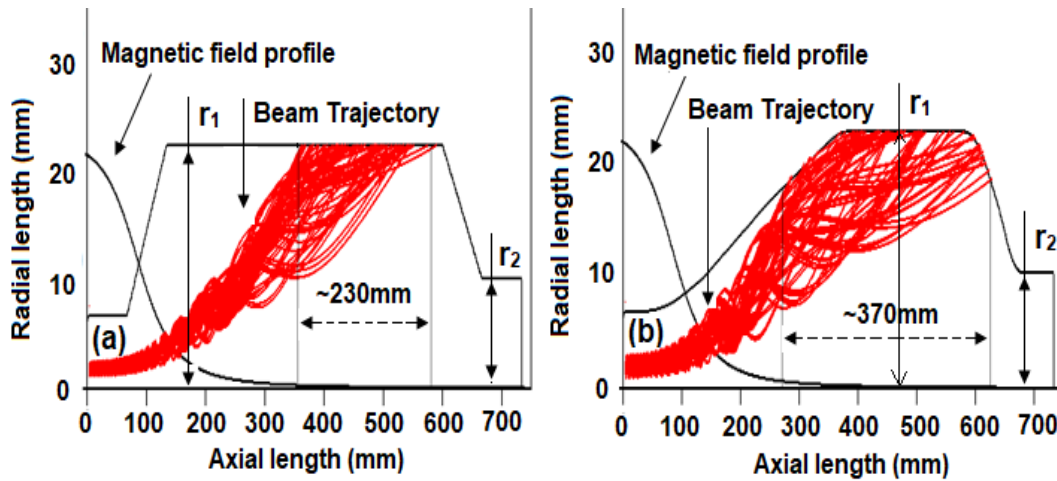
Figure 5.15 2D schematic, beam trajectory and magnetic field profile of (a) conventional type and (b) curved collector.
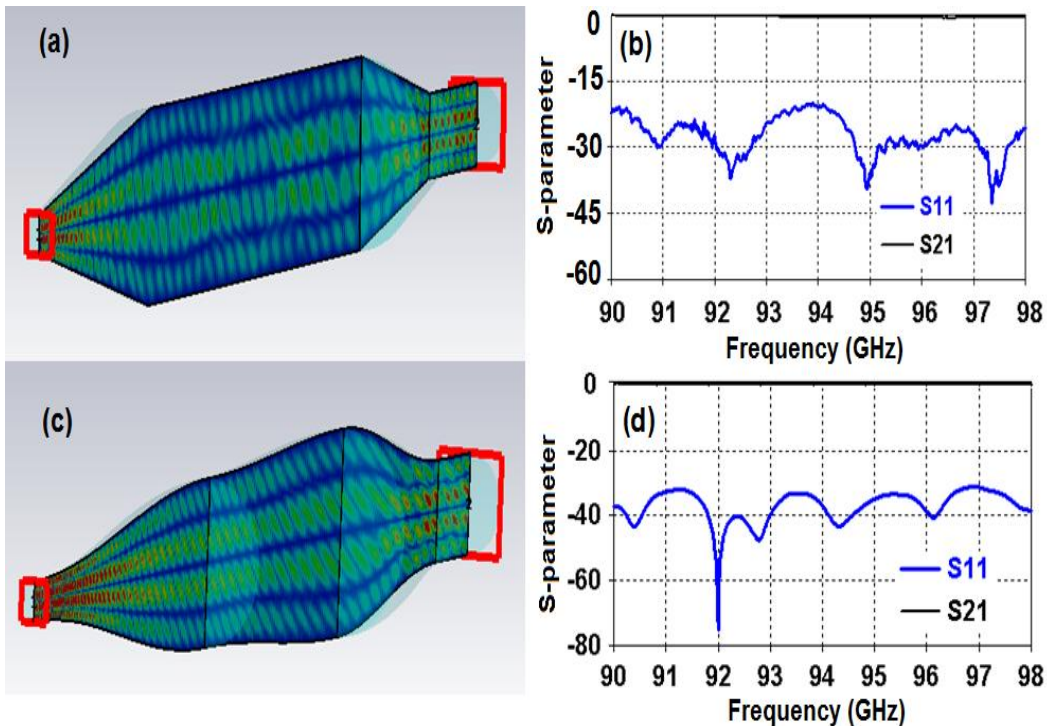

Figure 5.16 (a) The contour plot of TE_{02} mode electric field pattern and (b) S-parameter results for conventional collector, (c) the contour plot of TE_{02} mode electric field pattern and (d) S-parameter results for curved collector.

5.5.2. Double Disk Output Window

A double disk output window is designed and simulated to seal the vacuum from the outside atmospheric pressure and to extract the RF output with minimum reflection. The double disk window offers high transmission bandwidth and minimum reflection

116

than the single disk window [Lin (2007)]. In general, the material with high thermal conductivity, high mechanical strength and low loss tangent is chosen for the design of RF window. In the present study, the ceramic, Al_2O_3 with low loss tangent and permittivity of 9.7 is chosen due to its low cost and good mechanical strength [Donaldson *et al*. (2013)]. The propagation of the transfer electric modes through the window disk is considered using the boundary condition *i.e.,* the tangential field components are continuous at the disc surfaces. The reflection coefficient [Antonsen *et al*. (1992)] for the double disk window is defined as,

$$R = 2\left|\frac{\sin\theta \quad (\bar{\beta}^2 - 1)\left[(1+\bar{\beta})^2\cos(\theta+\gamma) - (1-\bar{\beta})^2\cos(\theta-\gamma)\right]^2}{\left[(1+\bar{\beta})^2 - (1-\bar{\beta})^2 e^{i2\theta}\right] - \left[(1-\bar{\beta})^2 - (1-e^{i2\theta})^2 e^{i2\gamma}\right]}\right| \qquad (5.10)$$

where, $\gamma \cong \beta_z d_1$, $\bar{\beta} = \beta_z'/\beta_z$, and $\theta = \beta_z' d$. $\beta_z' = \sqrt{(n\omega/c)^2 - k_{mn}^2}$ is the longitudinal wave number in the disc medium and n is the refractive index of the dielectric medium. $\beta_z = \sqrt{(\omega/c)^2 - k_{mn}^2}$ is the longitudinal wave number in an empty waveguide and 'd' is thickness of the disk. For minimum reflection at the output window, d should satisfy the condition: $\beta_z d = (2p+1)\pi/2$, where, p is an integer. The dependence of reflection coefficient on the disc thickness [Figure 5.17 (a)] shows that at d = 0.523mm and 1.05mm, the condition $\theta = \beta_z' d = m\pi$ is satisfied and R is observed as zero. In the present design d is chosen as 0.523mm and d_1 is 0.785mm. The transparency of the present RF window has been studied analytically by equation (5.10) and verified with its cold simulation using CST [Figure 5.17(b)]. Both the analytical and simulated results predicted a reflection coefficient better than -20dB over the frequency bandwidth of 15GHz and are found to be in close agreement. The CST model of present double disc window and its electric field contour plot of TE_{02} mode are also shown in the inset of [Figure 5.17(b)].
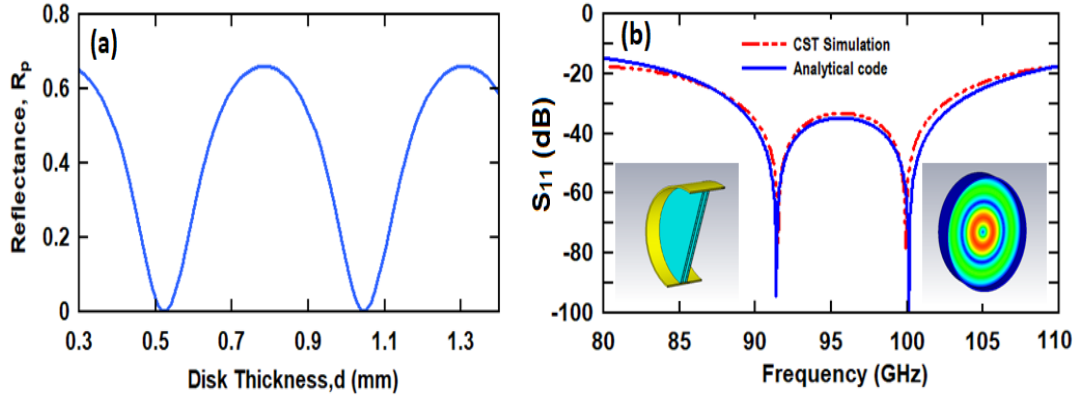
Figure 5.17 (a) Dependence of the R_p on the window disk thickness (d) for TE_{02} mode, (b) R_p Vs frequency for double disk window.

5.6.   Conclusion

The present work has been focused on the design and simulation studies of key sub-assemblies of second harmonic TE_{02} mode gyro-TWT. A triode type MIG has been designed and optimized for the present gyro-TWT to develop a gyrating electron beam with 4% axial velocity spread and velocity ratio of 1.22. A novel input coupler for TE_{02} mode has been designed and cold simulated to have ~0.8dB transmission loss and ~40dB reflection loss at the desired operating frequency. The periodic dielectric loaded RF interaction structure was designed and analyzed for its stability against BWOs. The PIC simulation of the present second harmonic dielectric loaded gyro-TWT predicted a peak RF output power of ~500kW at 91.4GHz in the desired operating TE_{02} mode. The calculated -3dB bandwidth and efficiency are ~3.6 GHz and ~20%, respectively. For the output section, an un-depressed curved collector has been designed to collect the spent electron beam. The heat wall loading of the collector was calculated as ~0.39kW /cm^2. A double disc window has been designed and its transmission behavior was calculated analytically and validated with "CST Microwave Studio".